Iridium Single Atoms Coupling with Oxygen Vacancies Boosts Oxygen Evolution Reaction in Acid Media

Jie Yin,[†] Jing Jin,[†] Min Lu,[†] Bolong Huang,*[,‡] Hong Zhang,[⊥] Yong Peng,[⊥] Pinxian Xi,*[,†] and Chun-Hua Yan[†]

[†]State Key Laboratory of Applied Organic Chemistry, Key Laboratory of Nonferrous Metal Chemistry and Resources Utilization of Gansu Province, College of Chemistry and Chemical Engineering, Lanzhou University, Lanzhou 730000, China.

[‡]Department of Applied Biology and Chemical Technology, The Hong Kong Polytechnic University, Hong Hum, Kowloon, Hong Kong SAR, China.

[⊥]Key Laboratory of Magnetism and Magnetic Materials of Ministry of Education, School of Physical Science and Technology, Lanzhou University, Lanzhou 730000, China.

KEYWORDS: Single atoms catalysts; nanosheets; oxygen vacancy; OER; acid media.

ABSTRACT: Simultaneous realization of improved activity, enhanced stability, and reduced cost remains a desirable yet challenging goal in the search of electrocatalysis oxygen evolution reaction (OER) in acid. Herein, we report a novel strategy to prepare iridium single-atoms (Ir−SAs) on ultrathin $NiCo_2O_4$ porous nanosheets (Ir−$NiCo_2O_4$ NSs) by co-electrodeposition method. The surface exposed Ir−SAs couplings with oxygen vacancy (V_O) and boosts the catalysts OER activity and stability in acid media. Their exhibit superior OER performance with an ultralow overpotential of 240 mV at j = 10 mA cm^{-2} and long-term stability of 70 h in acid media. The TOFs of 1.13 and 6.70 s^{-1} at an overpotential of 300 and 370 mV also confirm their remarkable performance. Density functional theory (DFT) calculations reveal that the prominent OER performance arises from the surface electronic exchange-and-transfer activities contributed by atomic Ir incorporation on the intrinsic V_O existed $NiCo_2O_4$ surface. The atomic Ir sites substantially elevate the electronic activity of surface lower coordinated Co-sites nearby V_O, which facilitate the surface electronic exchange-and-transfer capabilities. With this trend, the preferred H_2O-activation and stabilized *O have been reached towards competitively lower overpotential. This is a generalized key for optimally boosting OER performance.

Oxygen evolution reaction (OER) plays an important role in the sustainable development and energy conversion devices.[1−5] Unfortunately, the kinetics of OER is slow due to the four-electron/four-proton transition.[6,7] Therefore, great efforts have been devoted to design active and stable catalysts for OER.[8−10] Previous studies have demonstrated various excellent OER catalysts, such as gelled FeCoW oxyhydroxides,[11] Co_3O_4,[12] NiS_2/CoS_2−O NWs,[13] etc. Additionally, kinds of strategies, such as morphology,[14] electronic structure,[15] interface,[16] strain[17,18] etc., are developed to further improve the electrocatalytic performance of those catalysts. However, these reported catalysts are utilized only in alkaline media. The development of novel catalysts with superior OER activity and stability in acid media remains a challenge that requires more in-depth studies. Traditionally, Ir or ruthenium (Ru)-based nanomaterials show excellent activity for OER, but their stability is not very good in acid media.[19−21] Meanwhile, the high cost and low abundance severely impedes their large-scale application.[22] Thus, designing cost-effective and highly stable OER electrocatalysts becomes the pivotal task for future research.

Recently, single-atom catalysts (SACs) show an amazing electrocatalytic performance for many reactions,[23] especially for oxygen reduction reaction (ORR) and CO_2 reduction reaction (CO_2RR). With the unique structure based on metal coupling nitrogen (M−N_x) or metal coupling oxygen (M−O_x) and other coupling,[24] these ASCs show abundant exposed surface-active sites and ultralow metal content, suggesting higher metal utilization than usual nanocatalysts. Although those SACs have a such superior performance, successful synthesis those SACs still a challenge.[25] Generally, the SACs are prepared by high-temperature pyrolysis metal-doped zinc (Zn) 2-methylimidazolate framework (ZIF−8).[26] Therefore, we should pay attention to design facile strategy for preparing those SACs.

Herein, we developed Ir−SACs coupling with oxygen vacancies on $NiCo_2O_4$ NSs (Ir−$NiCo_2O_4$ NSs) by co-electrodeposition method. The Ir−$NiCo_2O_4$ NSs with porous ultrathin nanosheets morphology favor to expose active sites and create defects. Importantly, the Ir−$NiCo_2O_4$ NSs with abundant Ir−O_x active center and oxygen vacancies will exhibit boosting OER performance, especially in acid media. Density functional theory (DFT) calculations reveal that, the excellent OER performance arises from the high activities of electron exchange and transfer by the atomic Ir anchoring on the lower coordinated Co-sites nearby the V_O, which possess lower valence for efficient electron-transfer through overlapping with Fermi level. Especially, the anchored Ir-site plays an excellent protecting role for preventing the variation of Co valence state. Meanwhile, the anchored Ir-site also plays a distributary role for binding O and H species to reduce the deactivation of active-site coverage by over-binded O and H species on the Co-sites. From the atomic rearrangement perspective, the obtained Ir−$NiCo_2O_4$ NSs with abundant Ir−SAs coupling with oxygen vacancies exhibit activity and stability for OER in acid media (i.e., 0.5 M H_2SO_4). The

Ir−$NiCo_2O_4$ NSs catalyst shows an overpotential of 240 mV at a current density of 10 mA cm^{-2}. Significantly, the Ir−$NiCo_2O_4$ NSs also give a spectacular stability for OER in acid media. The Ir−$NiCo_2O_4$ NSs show slight potential decrease from 1.44 to 1.47 V after 70 h reaction at j = 10 mA cm^{-2}, indicating more superior stability than other recent reported OER catalysts in acid media. The Ir−$NiCo_2O_4$ NSs also display a high TOF of 1.13 and 6.70 s^{-1} at an overpotential of 300 and 370 mV for OER due to more efficient surface exposed Ir−O_x active center. Meanwhile, the Ir−$NiCo_2O_4$ NSs have an ultrahigh mass activity of 10.00 and 28.89 A mg_{Ir}^{-1} at an overpotential of 237 and 378 mV, which can be attributed to low Ir loading about 0.41%. This facile synthetic strategy prepares a promising SACs and offers a guideline for the fabrication of other metal-based SACs.

We developed co-electrodeposition method for synthesis the Ir−$NiCo_2O_4$ NSs (Figure S1). First, the Ir−NiCoLDH was deposited on carbon cloth used metal salt solution at −1.0 V vs. Ag/AgCl in three-electrode system for 15 min. Then, the Ir−NiCoLDH was annealed in air at 300 °C for 2 h to obtain $NiCo_2O_4$ and Ir−$NiCo_2O_4$ NSs. The X−ray diffraction (XRD) pattern (Figure 1a) of both $NiCo_2O_4$ and Ir−$NiCo_2O_4$ NSs match with cubic $NiCo_2O_4$ for a space group of F*3 (JCPDS No. 20−781, a = b = c = 8.11 Å). Obviously, there are no iridium oxides peaks appearing in Ir−$NiCo_2O_4$ NSs. Then, the scanning electron microscopy (SEM) is applied to characterize the morphology of the synthesized nanosheets. The $NiCo_2O_4$ exhibits a uniform nanosheet structure arraying on carbon cloth (Figure 1b). The transmission electron microscopy (TEM) shows a porous morphology of $NiCo_2O_4$ NSs (Figure 1c). The High-resolution transmission electron microscopy (HRTEM) also show the lattice fringes with interplanar distance of 0.245 nm, corresponding to the (311) crystallographic plane (Figure 1c). The corresponding FFT image (the insert in Figure 1c) show the exposed face of (311) and (220), respectively. For the same method, the Ir−$NiCo_2O_4$ also show a uniform nanosheets array on carbon cloth (Figure 1d). But the Ir−$NiCo_2O_4$ NSs show corrugated array and thinner nanosheets due to the surface modification by Ir−O_x species. TEM image (Figure 1e) also gives the porous nanosheets morphology of Ir−$NiCo_2O_4$ NSs. The elements mapping (Figure 1e) indicating the uniform distribution of Ir, Ni, Co and O in the selected nanosheets area. Similarly, the Inductively Coupled Plasma (ICP) test also shows existence of Ir in the obtained Ir−$NiCo_2O_4$ NSs with a low content about 0.41% (Table S1). The same with XRD data, the HRTEM and corresponding FFT images only show the structure information of $NiCo_2O_4$ without iridium oxides. The corresponding FFT image (the insert in Figure 1f) also gives the same crystallographic plane of (311), (220) and (440) for $NiCo_2O_4$, indicating the surface coupling Ir−O_x do not change the structure of $NiCo_2O_4$.

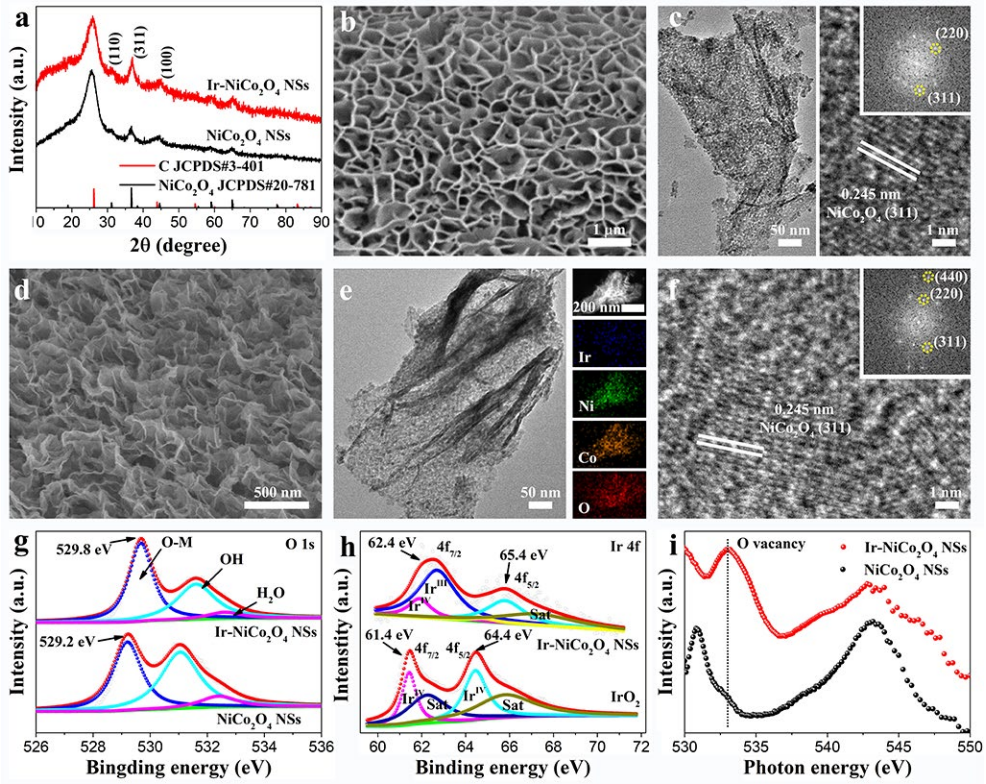

Figure 1. Characterization of $NiCo_2O_4$ and Ir−$NiCo_2O_4$ NSs. (a) XRD pattern of $NiCo_2O_4$ and Ir−$NiCo_2O_4$ NSs. (b, c) SEM, TEM and HRTEM images of $NiCo_2O_4$ NSs. The insert in (c) shows the corresponding FFT image of $NiCo_2O_4$ NSs. (d, e, f) SEM, TEM and HRTEM images of Ir−$NiCo_2O_4$ NSs. The insert in (f) shows the corresponding FFT image of Ir−$NiCo_2O_4$ NSs. (g) O 1s spectra of $NiCo_2O_4$ and Ir−$NiCo_2O_4$ NSs. (h) Ir 4f spectra of IrO_2 and Ir−$NiCo_2O_4$ NSs. (i) O−K edge XANES spectra of $NiCo_2O_4$ and Ir−$NiCo_2O_4$ NSs. In (i) the peak at 533 eV show the V_O.

Furthermore, the chemical and electronic states of $NiCo_2O_4$ and Ir−$NiCo_2O_4$ NSs were analyzed by various spectroscopy. As shown in Figure 1g, the O 1s X−ray photoelectron spectroscopy (XPS) spectra can be deconvoluted into three peaks:[27−29] lattice oxygen (M−O) at 529.8 eV, coordinatively oxygen vacancy or oxygen in hydroxyl group (V_O/OH) at 531.4 eV, and oxygen in adsorbed water (O−H_2O) at 532.5 eV. Compared with $NiCo_2O_4$ NSs, the banding energy of O 1s XPS spectra of Ir−$NiCo_2O_4$ NSs display a positive shift about 0.6 eV, which indicating a higher surface coupling after Ir−O_x created. Except the slight difference for O 1s spectra, the Ni and Co 2p spectrum of $NiCo_2O_4$ and Ir−$NiCo_2O_4$ NSs without obvious change (Figure S2), suggesting Ir−O_x species does not affect the substrate structure. Figure 1h compares the Ir 4f XPS spectra, commercial IrO_2 exhibits two peaks with Ir 4f doublet splitting energy of 3 eV for Ir $4f_{7/2}$ at 61.4 eV and Ir $4f_{5/2}$ at 64.4 eV,[28] while the peaks of Ir 4f spectrum for Ir−$NiCo_2O_4$ NSs clearly shift to higher binding energies, suggesting that the Ir

species on the surface of Ir−$NiCo_2O_4$ NSs mainly at +3 valence state. Additionally, the O 1s spectra indicate higher ratio of the oxygen species on the Ir−$NiCo_2O_4$ NSs surface that interact weakly with Ir as compared to that on rutile IrO_2 (Figure S3). The X−ray absorption near−edge structure (XANES) spectra of O K−edge show the oxygen vacancy for $NiCo_2O_4$ and Ir−$NiCo_2O_4$ NSs (Figure 1i), suggesting the abundant oxygen vacancies in Ir−$NiCo_2O_4$ NSs for big peak at 533 eV.[30] Meanwhile, the electron spin resonance (ESR) measurements were exploited to provide strong evidence for exploring the generation and variation of oxygen vacancies (Figure S4).[31] The Ir−$NiCo_2O_4$ NSs shows an stronger ESR signal than $NiCo_2O_4$ NSs, which is caused by electron trapped on surface oxygen vacancies.

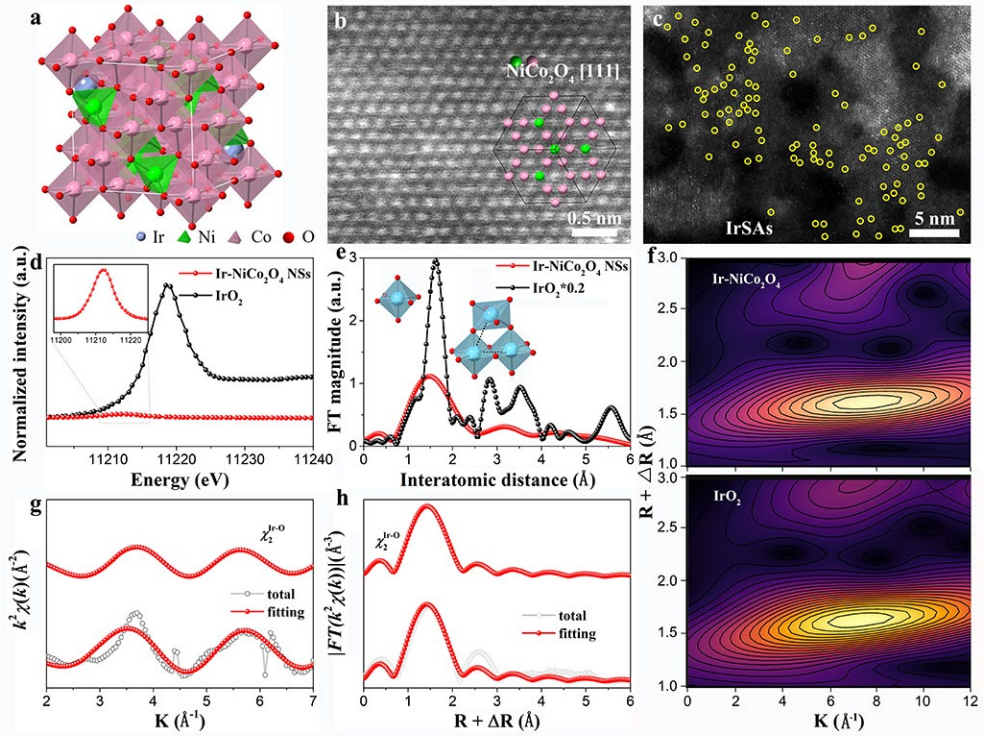

Figure 2. Structural characterization of Ir−$NiCo_2O_4$ NSs. (a) Structure of Ir−$NiCo_2O_4$ NSs. (b) HAADF-STEM image of Ir−$NiCo_2O_4$ NSs. The insert in (b) show the corresponding crystal structure of $NiCo_2O_4$ unit cells taken along the [111] orientation. (c) the HAADF-STEM image of Ir−$NiCo_2O_4$ NSs, indicating the Ir−SAs. (d) XANES spectra for IrO_2 and Ir−$NiCo_2O_4$ NSs. (e) EXAFS spectra for IrO_2 and Ir−$NiCo_2O_4$ NSs. (f) the corresponding wavelet transforms for the k^3−weighted Ir L3−edge EXAFS signals of Ir−$NiCo_2O_4$ NSs and commercial IrO_2. (g, h) Ir L3−edge EXAFS of Ir−$NiCo_2O_4$ NSs in k (g) and R (h) spaces, which curve is Ir–O backscattering signals (χ_2) included in the fit (red line) and experimental signal (black line). The measured and calculated spectra show excellent agreement.

The Ir−O_x species in Ir−$NiCo_2O_4$ NSs was further studied to confirm their chemical environment. As shown in Figure 2a, the spinel structure with oxygen vacancies coupled Ir−SAs was built. The DFT calculation has been demonstrated that the surface with oxygen vacancies is much more activate for the electrons neighboring the oxygen vacancy previously occupied the O 2p orbital become delocalized.[27] Then, the high angle annular darkfield scanning transmission electron microscope (HAADF-STEM) was used to further confirm the structure of Ir−$NiCo_2O_4$ NSs. The substrate $NiCo_2O_4$ gives a unit cells taken along the [111] orientation (Figure 2b). On this basis, aberration corrected HAADF-STEM was further utilized for a direct discernment of the Ir distribution. The result displays plenty of speckled bright dots in the high-resolution HAADF-STEM image (Figure 2c), which strongly confirms the atomic isolation of Ir−SAs in the obtained Ir−$NiCo_2O_4$ NSs. By contrast, the commercial IrO_2 sample has a bad morphology with an exposed (110) crystallographic plane (Figure S5).

The XANES (Figure 2d) and extended X−ray absorption fine structure (EXAFS) spectra (Figure 2d) were employed to demonstrate the atomic coordination environment of atomically dispersed Ir in Ir−$NiCo_2O_4$ NSs. Commercial IrO_2 was used as benchmarks. The XANES spectra demonstrates that the intensity of Ir−$NiCo_2O_4$ NSs is much lower than that of commercial IrO_2, meanwhile the peak of Ir−$NiCo_2O_4$ NSs show a negative shift, indicating the decreased valence state of Ir in Ir−$NiCo_2O_4$ NSs (Figure 2d). In the Fourier transforms (FTs, R−space, Figure 2e) for EXAFS, both Ir−$NiCo_2O_4$ NSs and IrO_2 show a single prominent peak located at about 1.5 Å ascribed to the Ir−O scattering path. It should be mentioned that the spectra here were plotted without phase correction, so the distance is a little bit shorter than that of the typical distance of 2.0 Å in the [IrO_6] octahedron.[32] Additionally, the second Ir−Ir^I shell and the third Ir−Ir^{II} shell are also clearly observable in commercial IrO_2, while we cannot find the peaks of second and third Ir−Ir shell in Ir−$NiCo_2O_4$ NSs. Thus, it is concluded that Ir−$NiCo_2O_4$ NSs only has the Ir–O scattering path, which is also consistent with the HAADF-STEM images. Apart from that, EXAFS wavelet transform (WT) analysis (Figure 2f) was performed for further confirmation of the atomic Ir dispersion, due to its capability of discriminating the backscattering atoms by providing not only radial distance resolution but also k−space resolution.[33,34] In line with the FTs, the WT analysis of Ir−$NiCo_2O_4$ NSs reveals only one intensity maximum at approximately 7.8 $Å^{-1}$ similarly with that observed in commercial IrO_2, suggesting the complete absence of crystalline Ir−Ir structures. The coordination configuration in Ir−$NiCo_2O_4$ NSs was further investigated by quantitative least-squares EXAFS curve-fitting analysis using Ir−O backscattering path (Figure 2g, h and Table S2). The best fitting analysis shows clearly that the main peak at 1.5 Å originates from Ir−O shell with a coordination number of 4.05. Whereas the commercial IrO_2 fitting analysis using Ir−O and Ir−Ir backscattering path displays a coordination number of 4.71 for Ir−O and 5.46 for Ir−Ir shell (Figure S6 and Table S2).

We also studied the chemical environment of Ni and Co after the fabrication of Ir−SAs on the $NiCo_2O_4$ NSs surface. Comparing with $NiCo_2O_4$ NSs, the EXAFS spectrum at Ni k−edge (Figure S7) of Ir−$NiCo_2O_4$ NSs shows similar intensity and peaks position, which indicating the surface Ir−SAs have no effect for Ni coordination environment. The fitting results (Figure S8 and Table S3) also show the similar coordination number of Ni−O and Ni−Ni/Co. Although the peaks position of EXAFS spectrum at Co k-edge (Figure S9) still the same, the intensity of Co−O enhanced after building the surface Ir−SAs, suggesting the bigger coordination number of Co−O (5.02) in Ir−$NiCo_2O_4$ NSs (Figure S10 and Table S4). Furthermore, we fabricated other Ir−SAs on $NiCo_2O_4$ NSs at 400 and 500 °C and found that Ir−O_x active species can be easily obtained at 300 °C, which can be attributed to the abundant oxygen vacancies more active at 300 °C. Based on the same method, the obtained Ir−$NiCo_2O_4$ NSs at 400 and 500 °C still have porous nanosheets morphology (Figure S11). Additionally, the XANES spectra at both Ni and Co k−edge (Figure S12) show higher photon energy with a positive shift after higher temperature annealing, which indicating the enhanced valence state of Ni and Co and decreased oxygen vacancies at higher temperature.[35] Meanwhile, the EXAFS at R−space (Figure S13) of Ni and Co show improved intensity at high temperature, suggesting the enhanced coordination number. Additionally, the XPS spectra were used to confirm the valence state change after different temperature treatment. According to Ni 2p (Figure S14) and Co 2p (Figure S15) spectra of Ir−$NiCo_2O_4$ NSs, the calculated results show increased valence state at high temperature for Ni^{3+}/Ni^{2+} from 0.45 to 0.87 and Co^{3+}/Co^{2+} from 1.5 to 2.0, respectively. After 400 and 500 °C annealing, the Ir species on the surface of $NiCo_2O_4$ NSs are at the +4 valence state higher than +3 valence state of Ir obtained at 300 °C (Figure S16). The O 1s spectra also show enhanced O−M bond after higher temperature with the increased ratio of OM/OOH from 1.03 to 1.40 (Figure S17), suggesting the decrease of oxygen vacancies at high temperature.

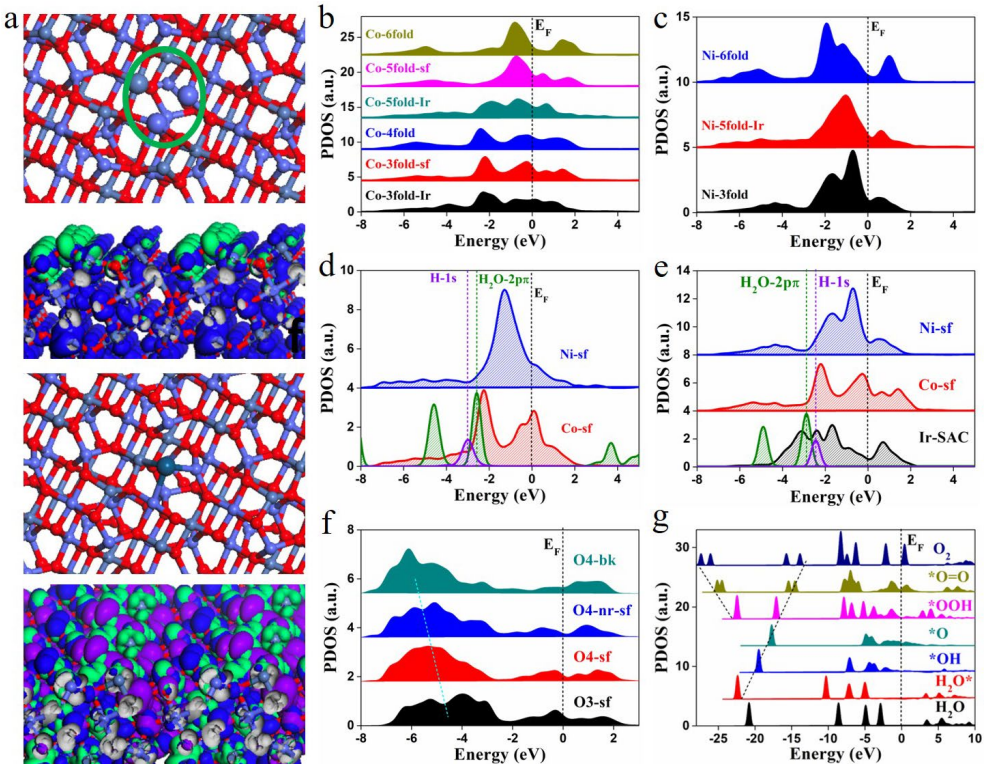

Figure 3. Theoretical interpretations of Electronic activities for acidic OER. (a) The top view of surface $NiCo_2O_4$ with V_O; the side view of surface electronic orbital contour plot of $NiCo_2O_4$ with V_O; the atomic Ir anchored near the V_O site on the $NiCo_2O_4$ surface; and the side view of modified orbital contour plot of the Ir−$NiCo_2O_4$−VO. (b) PDOSs of Co−3d bands from bulk lattice towards surface region. (c) PDOSs Ni−3d band from bulk lattice towards surface region. (d) The p−d orbital alignment of surface Ni and Co sites for plain $NiCo_2O_4$ with V_O. (e) The p−d orbital alignment of surface Ni, Co, and Ir sites for Ir−$NiCo_2O_4$−V_O. (f) PDOSs of lattice O−2p bands from bulk lattice towards surface region. (g) PDOSs of O−2p bands for the intermediate O−species.

We now interpret the mechanism for predicted acidic OER performance of atomic Ir anchored $NiCo_2O_4$ with V_O. The active bonding and anti-bonding orbital near the Fermi level (EF) indicates the anchored Ir single atomic sites evidently modify the surface electronic distribution, which is given by the low coordinated Ni−Co sites nearby the V_O with weakly d−d coupled (Figure 4a). For the PDOSs of 3d−bands of different Co-sites form the system, the 3-fold coordinated Co nearby the Ir-site across EF with uniformly merged e_g and t_{2g} components, where the d-band center has shifted towards higher position close to EF. On the contrast, from surface towards bulk layer, the higher coordinated Co-sites present underperformed electronic activities either showing less population near EF or with less overlapping with EF for electron-transfer. Therefore, the role of Ir-site substantially improves the electronic activity of surface lower coordinated Co-sites for efficient electron-exchange and transfer (EXT) capability (Figure 4b). For the PDOSs of 3d-band of various Ni-sites, the d-orbital modification given by Ir-site is rather limited, the d-band centers remain nearly unchanged. This potentially indicates the surface Ni-sites are play a significant role of stabilizing the local electron-transfer environment nearby Co-sites, which stabilizes the valance states of surface Co-sites (Figure 4c). For the roles of active sites, the Ir−5d band exhibits substantially wide range for optimally overlapping with H_2O−2pπ and H−1s orbitals. Meanwhile, the surface Co−3d band has also shown excellent overlapping with H_2O−2pπ and H−1s orbitals. Therefore, the anchored Ir-site plays an excellent protecting role for preventing the variation of Co valence state. The anchored Ir-site also plays a distributary role for binding O and H species to reduce the deactivation of active-site by intermediates over-binding on the Co-sites (Figure 4d&e). The lattice

O−2p band PDOSs analysis demonstrate a trend that the surface O-sites possess highest p-band center with higher overlapping degree with EF for active electron-transfer between surface Ni and Co sites (Figure 4f). Further on the PDOSs of the O-intermediates, there has been a linear trend from adsorbing H_2O towards the [*OOH] and [*O=O], indicating an optimal balance between electron-transfer adsorption energetic preference has been guaranteed for substantially efficient OER yield rate and catalysis performance (Figure 4g).

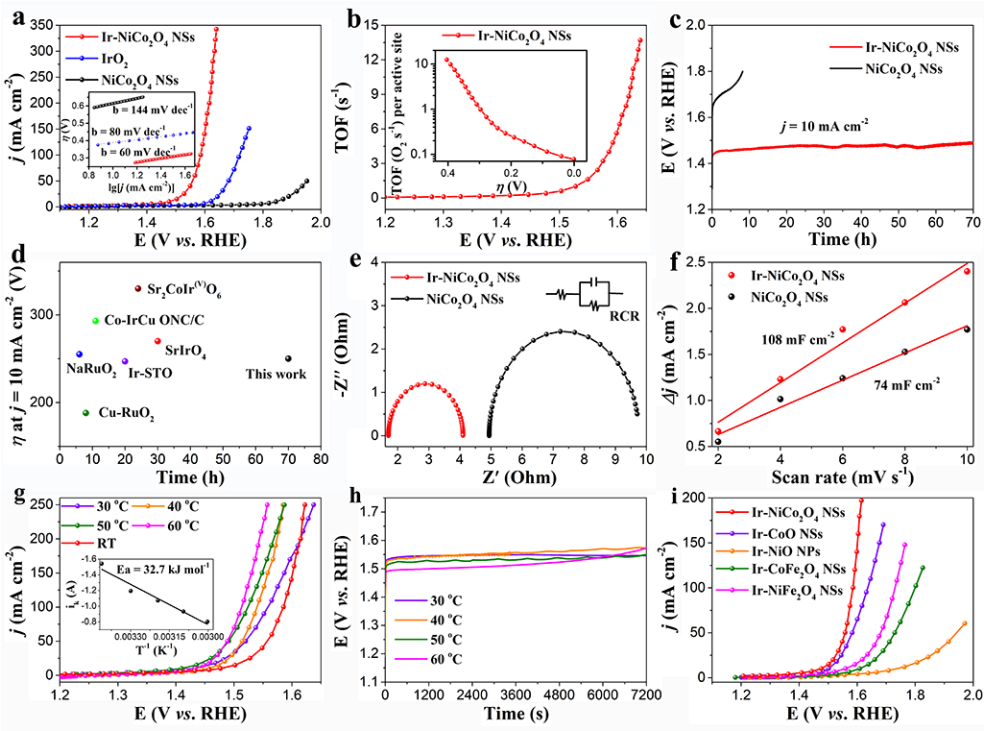

Figure 4. Catalytic performance of $NiCo_2O_4$ NSs, Ir−$NiCo_2O_4$ NSs and commercial IrO_2. (a) LSV curves of commercial IrO_2, $NiCo_2O_4$ and Ir−$NiCo_2O_4$ NSs in 0.5 M H_2SO_4. The insert in (a) shows the corresponding Tafel plots. (b) TOF curve of Ir−$NiCo_2O_4$ NSs for OER. The insert in (b) shows the corresponding TOF plot. (c) Chronoamperometric response of $NiCo_2O_4$ and Ir−$NiCo_2O_4$ NSs for OER at 10 mA cm^{-2} in 0.5 M H_2SO_4. (d) EIS curves of $NiCo_2O_4$ and Ir−$NiCo_2O_4$ NSs in 0.5 M H_2SO_4. (e) Compared overpotential at j = 10 mA cm^{-2} and stability of Ir−$NiCo_2O_4$ NSs with previously reported OER catalysts in acid media. (f) The changing current density differences (Δj) plotted against scan rates for $NiCo_2O_4$ and Ir−$NiCo_2O_4$ NSs. (g) The LSV curves of Ir−$NiCo_2O_4$ NSs for OER at different temperature. The inset in (g) shows Arrhenius plot of the kinetic current at η = 300 mV. (h) Chronoamperometric response of Ir−$NiCo_2O_4$ NSs for OER at 10 mA cm^{-2} in 0.5 M H_2SO_4 under different temperature. (i) The LSV curves of Ir SAs on different oxides substrate for OER in 0.5 M H_2SO_4.

The electrocatalytic performances of the prepared NSs are evaluated by the linear scan voltammogram (LSV) in N_2−saturated 0.5 M H_2SO_4 solution at room temperature. Figure 3a shows the OER performance of those NSs. As expected, Ir−$NiCo_2O_4$ NSs displays the best OER performance with the onset potential of 180 mV (vs. RHE) and overpotential of 240 mV at the current density of 10 mA cm^{-2} much better than those of commercial IrO_2 (290 mV and 370 mV) and $NiCo_2O_4$ NSs only show negligible OER performance. Due to the decreased Ir−O_x active center and oxygen vacancies, the catalytic activity of the Ir−$NiCo_2O_4$ NSs obtained at 300 °C is the best among all Ir−$NiCo_2O_4$ NSs at different temperature (Figure S18). The Ir−$NiCo_2O_4$ NSs obtained at 300 °C also displays the smallest Tafel plot of 60 mV dec^{-1} in all catalysts, demonstrating the fastest OER kinetics. It is well known that the turnover frequencies (TOF), responding to the intrinsic per-site activity of a catalyst, is the best figure of merit for comparing activities among different catalysts.[36–38] Herein, the TOF per metal site are calculated based on the hypothesis that all Ir−O_x active center was accessible to the electrolyte. Accordingly, the TOF values per Ir site of Ir−$NiCo_2O_4$ NSs were calculated. In particular, the TOFs of Ir−$NiCo_2O_4$ NSs are 1.13 and 6.70 O_2 per s at an overpotential of 300 and 370 mV, respectively. TOF plots against the applied overpotential are summarized (insert in Figure 3b), demonstrating the linearly increasing TOF from 0.25 to 0.4 V. For low loading Ir−SAs, the mass activity of Ir−$NiCo_2O_4$ NSs is very huge about 10.00 and 28.89 A mg_{Ir}^{-1} at an overpotential of 237 and 378 mV, respectively (Figure S19). In particular, for the purpose of direct illustration, the boosted OER performance of Ir−$NiCo_2O_4$ NSs, the overpotential, mass activity, stability and TOF values of several Ir and Ru based OER catalysts, such as amorphous Li−IrO_x,[28] $CaCu_3Ru_4O_{12}$,[39] RuO_2 nanosheets,[40] $Y_2Ru_2O_{7-\delta}$,[41] Ru_1−Pt_3Cu,[42] Ba_2YIrO_6 DPs,[43] $IrO_x/SrIrO_3$[44] are summarized (Table S5). Importantly, the Ir−$NiCo_2O_4$ NSs shows excellent stability for OER about 70 h in acid media at current densities of 10 mA cm^{-2} with slight potential change from 1.44 to 1.47 V (Figure 3c). After long-term stability test, we further researched the composition, morphology and electronic structure of Ir−$NiCo_2O_4$ NSs. The XRD pattern without obvious change after stability test (Figure S20), indicating that $NiCo_2O_4$ not completely dissolved in 0.5 M H_2SO_4. The nanosheets arrays morphology of Ir−$NiCo_2O_4$ NSs first was confirmed by SEM (Figure S21). Additionally, the TEM image (Figure S22a) also shows the porous nanosheets morphology of Ir−$NiCo_2O_4$ NSs after OER in acid media, the HRTEM (Figure S22b) also give the (311) and the elements mapping (Figure S22c) show the uniform distribution of Ir, Ni, Co, O, respectively. The elements content and valence state were studied by ICP, energy dispersive spectrometer (EDS) and XPS. Compared with the initial content, after OER measurement, the content of Ni and Co decreased (Table S6) for the acid corrosion, while the SEM-EDS tests also indicating the decreased Co/Ni and enhanced Ir content in Ir−$NiCo_2O_4$ NSs after OER in acid (Figure S23). More importantly, the enhanced content of oxygen further indicating the created surface reconstruction of Ir−O_x, which is key part for the superior OER stability of Ir−$NiCo_2O_4$ NSs in acid media. The electronic structure of Ir 4f, Ni 2p, Co 2p and O 1s no change for the XPS spectra of each element does

not have a shift (Figure S24). The ultrahigh activity and stability of Ir−$NiCo_2O_4$ NSs is outstanding among those Ir/Ru-based acid OER catalysts (Figure 3d).

For the Ir−O_x species built on the surface of $NiCo_2O_4$ NSs, the electrochemical impedance spectroscopy (EIS) analysis (Figure 3e) shows electronic conductivity of Ir−$NiCo_2O_4$ NSs enhanced with low solution resistance (R_s) of 1.7 Ohm and charge-transfer resistance (R_{ct}) of 2.1 Ohm (Table S7). Based on their NSs array structure, we further tested the electrochemical double layer capacitance (C_{dl}) to evaluate the electrochemical surface area (ECSA) of the catalysts (Supplementary Figure 25).[45] The C_{dl} of Ir−$NiCo_2O_4$ NSs is 108 mF cm^{-2} higher than that of $NiCo_2O_4$ NSs (74 mF cm^{-2}) (Figure 3f), meanwhile the calculated ECSA is 1800 cm^2 for Ir−$NiCo_2O_4$ NSs and 1233 cm^2 for $NiCo_2O_4$ NSs (Table S8), indicating their larger active surface area. Furthermore, to assess the kinetic barriers involved in OER, we studied the effect of temperature on the performance of Ir−$NiCo_2O_4$ NSs in acid media (Figure 3g).[11] The Arrhenius plot at η = 300 mV for Ir−$NiCo_2O_4$ NSs (insert in Figure 3g) demonstrates low apparent barrier value of 32.7 kJ mol^{-1}. Additionally, the stability of Ir−$NiCo_2O_4$ NSs for OER in acid under different temperature tests indicate the excellent stability for Ir−$NiCo_2O_4$ NSs at high temperature (Figure 3h). More importantly, we used same co−electrodeposition method built various oxides loaded Ir−SAs (Figure S26). They show different OER performance in acid media (Figure 3i), in which $NiCo_2O_4$ and CoO with NSs morphology should better performance suggesting the NSs is good for Ir−SAs coupling on oxygen vacancies.

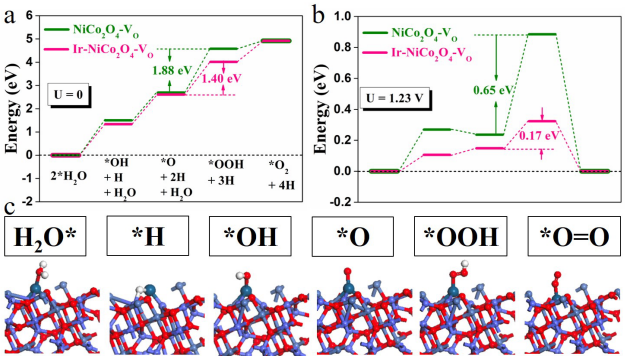

Figure 5. OER pathway within acidic condition. (a) The pathways of both four-electron based alkaline OER at U = 0 V. (b) The OER pathways are summarized at U = 1.23 V. (c) Local structural configurations of initial reactant, intermediates or final product on the Ir−$NiCo_2O_4$−V_O.

We move onto the energetic pathway of acidic OER for the system (Figure 5). It shows that under U = 0 V (standard potential), the potential determining step (PDS) is the formation of the [*OOH] from the step of [*O] state. The Ir−atomic site incorporated $NiCo_2O_4$ with V_O lowers the barrier (1.40 eV) compared to the one (1.88 eV) in plain $NiCo_2O_4$ with V_O (Figure 5a). At the U = 1.23 V, the different energetic trends become obviously. The atomic Ir ameliorates the initial splitting barrier (0.12 eV) for [*OH] formation, which is nearly two times lower than the barrier (0.27 eV) in plain $NiCo_2O_4$ with V_O. Furthermore, the stable [*O] formation from the system of Ir incorporated $NiCo_2O_4$ with V_O determines the formation of [*OOH] with barrier of 0.17 eV as well as the overpotential is 0.17 V (i.e. max{[barrier-1.23 eV]/e}), which is almost four times lower than the plain $NiCo_2O_4$ with V_O, in a good agreement with experimental trend (Figure 5b). Further structural evolution displays that the surface Ir atomic site incorporation at the lower coordinated Ni and Co sites not only energetically favored environments for initial H_2O adsorption and further splitting activation, but also enhances the valence stability between Ir and Co sites associated by efficient electron-transfer (Figure 5c). Therefore, both electronic and energetic properties have been discussed and consistently aligned the energetically favorable OER performance given by the Ir−$NiCo_2O_4$−V_O system.

In this work, we developed co-electrodeposition strategy to fabricate Ir−SACs coupling with oxygen vacancies on $NiCo_2O_4$ NSs (Ir−$NiCo_2O_4$ NSs), which exhibit boosting OER performance in acid media. For example, the Ir−$NiCo_2O_4$ NSs catalyst shows ultralow overpotential of 240 mV at j = 10 mA cm^{-2} and long-term stability for 70 h, demonstrating more superior activity and stability than other recent reported acid OER catalysts. What'smore, the Ir−$NiCo_2O_4$ NSs also exhibit an ultrahigh TOF of 1.13 and 6.70 s^{-1} at an overpotential of 300 and 370 mV for OER and mass activity of 10.00 and 28.89 A mg_{Ir}^{-1} at an overpotential of 237 and 378 mV. DFT calculations reveal that, the surface atomic Ir anchored Co-sites nearby V_O achieve high electron exchange and transfer activities. More importantly, the surface Ir atomic site incorporation at the lower coordinated Ni and Co sites not only energetically favored environments for initial H_2O adsorption and further splitting activation, but also enhances the valence stability of Co sites associated by efficient electron-transfer. This synergetic mutual activation between Ir and Co sites plays a key role for alleviating the over-oxidation or valence instabilities of plain Co sites from conventional $NiCo_2O_4$ catalytic system. The designed strategy gives a promising way to prepare 2D metal nanomaterials with unsaturated metallic surface, which will enhance the intrinsic activity and selective and can be used in various energy conversion reactions.

ASSOCIATED CONTENT

Supporting Information

The Supporting Information is available free of charge on the ACS Publications website.

Detailed methods (synthesis, characterization, electrochemistry, and DFT calculations) and corresponding additional data (PDF)

AUTHOR INFORMATION

Corresponding Author

*xipx@lzu.edu.cn. (P.Xi)
*bhuang@polyu.edu.hk. (B.Huang)

Author Contributions

[#]These authors contributed equally to this work.

Notes

Any additional relevant notes should be placed here.

ACKNOWLEDGMENT

We acknowledge support from the National Natural Science Foundation of China (NO. 21931001, 21922105, 21571089), the Fundamental Research Funds for the Central Universities (lzujbky-2018-k08, lzujbky-2016-k02, lzujbky-2018-it40 and lzujbky-2017-it42). Special Fund Project of Guiding Scientific and Technological Innovation Development of Gansu Province (2019ZX-04). Bolong Huang acknowledges the support of the Natural Science Foundation of China (NSFC) (No.: 21771156), and the Early Career Scheme (ECS) fund (Grant No.: PolyU 253026/16P) from the Research Grant Council (RGC) in Hong Kong.

REFERENCES

(1) Turner, J. A. Sustainable hydrogen production. Science **2004**, *305*, 972−974.

(2) Suntivich, J.; Gasteiger, H. A.; Yabuuchi, N.; Nakanishi, H.; Goodenough, J. B.; Yang, S.-H. Design principles for oxygen-reduction activity on perovskite oxide catalysts for fuel cells and metal–air batteries. Nat. Chem. **2011**, *3*, 546−550.

(3) Debe, M. K. Electrocatalyst approaches and challenges for automotive fuel cells. Nature **2012**, *486*, 43−51.

(4) Ma, T.; Dai, S.; Jaroniec, M.; Qiao, S. Metal-Organic Framework Derived Hybrid Co_3O_4-Carbon Porous Nanowire Arrays as Reversible Oxygen Evolution Electrodes. *J. Am. Chem. Soc.* **2014**, *136*, 13925−13931.

(5) Zhu, Y.; Ma, T. Y.; Jaroniec, M.; Qiao, S. Z. Self‐Templating Synthesis of Hollow Co_3O_4 Microtube Arrays for Highly Efficient Water Electrolysis. *Angew. Chem. Int. Ed.* **2017**, *56*, 1324−1328.

(6) Xu, K.; Chen, P.; Li, X.; Tong, Y.; Ding, H.; Wu, X.; Chu, W.; Peng, Z.; Wu, C.; Xie, Y. Metallic Nickel Nitride Nanosheets Realizing Enhanced Electrochemical Water Oxidation. *J. Am. Chem. Soc.* **2015**, *137*, 4119−4125.

(7) Bediako, D.; Lassalle-Kaiser, B.; Surendranath, Y.; Yano, J.; Yachandra, V.; Nocera, D. Structure-Activity Correlations in a Nickel-Borate Oxygen Evolution Catalyst. *J. Am. Chem. Soc.* **2012**, *134*, 6801−6209.

(8) Zheng, Y.; Jiao, Y.; Zhu, Y.; Cai, Q.; Vasileff, A.; Li, L. H.; Han, Y.; Chen, Y.; Qiao, S.-Z. Molecule-Level gC_3N_4 Coordinated Transition Metals as a New Class of Electrocatalysts for Oxygen Electrode Reactions. *J. Am. Chem. Soc.* **2017**, *139*, 3336−3339.

(9) Feng, L-L.; Yu, G.; Wu, Y.; Li, G.-D.; Li, H.; Sun, Y.; Asefa, T.; Chen, W.; Zou, X. High-Index Faceted Ni_3S_2 Nanosheet Arrays as Highly Active and Ultrastable Electrocatalysts for Water Splitting. *J. Am. Chem. Soc.* **2015**, *137*, 14023−14026.

(10) Gao, M.; Sheng, W.; Zhuang, Z.; Fang, Q.; Gu, S.; Jiang, J.; Yan, Y. Efficient Water Oxidation Using Nanostructured α-Nickel-Hydroxide as an Electrocatalyst. *J. Am. Chem. Soc*. **2014**, *136*, 7077−7084.

(11) Zhang, B.; Zheng, X.; Voznyy, O.; Comin, R.; Bajdich, M.; García-Melchor, M.; Han, L.; Xu, J.; Liu, M.; Zheng, L.; de Arquer, F. P. G.; Dinh, C. T.; Fan, F.; Yuan, M.; Yassitepe, E.; Chen, N.; Regier, T.; Liu, P.; Li, Y.; Luna, P. D.; Janmohamed, A.; Xin, H. L.; Yang, H.; Vojvodic, A.; Sargent, E. H. Homogeneously dispersed multimetal oxygen-evolving catalysts. *Science* **2016**, *352*, 333−337.

(12) Koza, A. J.; He, Z.; Miller, S.; Switzer, A. Electrodeposition of Crystalline Co3O4 a Catalyst for the Oxygen Evolution Reaction. *J. Chem. Mater.* **2012**, *24*, 3567−3573.

(13) Yin, J.; Li, Y.; Lv, F.; Lu, M.; Sun, K.; Wang, W.; Wang, L.; Cheng, F.; Li, Y.; Xi, P.; Guo, S. Oxygen Vacancies Dominated NiS_2/CoS_2 Interface Porous Nanowires for Portable Zn–Air Batteries Driven Water Splitting Devices. *Adv. Mater*. **2017**, *29*, 1704681.

(14) Lei, F.; Sun, Y.; Liu, K.; Gao, S.; Liang, L.; Pan, B.; Xie, Y. Oxygen vacancies confined in ultrathin indium oxide porous sheets for promoted visible-light water splitting. *J. Am. Chem. Soc.* **2014**, *136*, 6826−6829.

(15) Yin, J.; Jin, J.; Zhang, H.; Lu, M.; Peng, Y.; Huang, B.; Xi, P.; Yan, C.-H. Atomic Arrangement in Metal-Doped NiS_2 Boosts the Hydrogen Evolution Reaction in Alkaline Media. *Angew. Chem. Int. Ed*. **2019**, *58*, 18676−18682.

(16) Yin, J.; Li, Y.; Lv, F.; Fan, Q.; Zhao, Y.-Q.; Zhang, Q.; Wang, W.; Cheng, F.; Xi, P.; Guo, S. NiO/CoN Porous Nanowires as Efficient Bifunctional Catalysts for Zn−Air Batteries. *ACS Nano* **2017**, *11*, 2275−2283.

(17) Bu, L.; Zhang, N.; Guo, S.; Zhang, X.; Li, J.; Yao, J.; Wu, T.; Lu, G.; Ma, J.-Y.; Su, D.; Huang, X. Biaxially strained PtPb/Pt core/shell nanoplate boosts oxygen reduction catalysis. *Science* **2016**, *354*, 1410−1414.

(18) Cheng, W.; Zhao, X.; Su, H.; Tang, F.; Che, W.; Zhang, H.; Liu, Q. Lattice-strained metal-organic-framework arrays for bifunctional oxygen electrocatalysis. *Nat. Energy* **2019**, *4*, 115−122.

(19) Jiao, Y.; Zheng, Y.; Jaroniec, M.; Qiao, S. Z. Design of electrocatalysts for oxygen-and hydrogen-involving energy conversion reactions. *Chem. Soc. Rev.* **2015**, *44*, 2060−2086.

(20) Duan, J.; Chen, S.; Vasileff, A.; Qiao, S. Z. Anion and cation modulation in metal compounds for bifunctional overall water splitting. *ACS Nano* **2016**, *10*, 8738−8745.

(21) Zhu, Y. P.; Guo, C.; Zheng, Y.; Qiao, S.-Z. Surface and interface engineering of noble-metal-free electrocatalysts for efficient energy conversion processes. *Acc. Chem. Res*. **2017**, *50*, 915−923.

(22) Wu, T.; Sun, S.; Song, J.; Xi, S.; Du, Y.; Chen, B.; Sasangka, W. A.; Liao, H.; Gan, C. L.; G. Scherer, G.; Zeng, L.; Wang, H.; Li, H.; Grimaud, A.; J. Xu, Z. Iron-facilitated dynamic active-site generation on spinel $CoAl_2O_4$ with self-termination of surface reconstruction for water oxidation. *Nat. Catal*. **2019**, *2*, 763−772.

(23) Wang. A.; Li, J.; Zhang, T. Heterogeneous single-atom catalysis. *Nat. Rev. Chem*. **2018**, *2*, 65−81.

(24) Cao, L.; Luo, Q.; Liu, W.; Lin, Y.; Liu, X.; Cao, Y.; Zhang, W.; Wu, Y.; Yang, J.; Yao, T.; Wei, S. Identification of single-atom active sites in carbon-based cobalt catalysts during electrocatalytic hydrogen evolution. *Nat. Catal.* **2019**, *2*, 134−141.

(25) Lang, R.; Xi, W.; Liu, J.-C.; Cui, Y.-T.; Li, T.; Lee, A. F.; Chen, F.; Chen, Y.; Li, L.; Li, L.; Li, J.; Miao, S.; Liu, X.; Wang, A.-Q.; Wang, X.; Luo, J.; Qiao, B.; Li, J.; Zhang, T. Non defect-stabilized thermally stable single-atom catalyst. *Nat. commun.* **2019**, *10*, 1−10.

(26) Zhang, M.; Wang, Y.-G.; Chen, W.; Dong, J.; Zheng, L.; Luo, J.; Wan, J.; Tian, S.; Cheong, W.-C.; Wang, D.; Li, Y. Metal (hydr) oxides@ polymer core–shell strategy to metal single-atom materials. *J. Am. Chem. Soc.* **2017**, *139*, 10976−10979.

(27) Bao, J.; Zhang, X.; Fan, B.; Zhang, J.; Zhou, M.; Yang, W.; Hu, X.; Wang, H.; Pan, B.; Xie, Y. Ultrathin spinel-structured nanosheets rich in oxygen deficiencies for enhanced electrocatalytic water oxidation. *Angew. Chem., Int. Ed.* **2015**, *54*, 7399−7404.

(28) Gao, J.; Xu, C.-Q.; Hung, S.-F.; Liu, W.; Cai, W.; Zeng, Z.; Jia, C.; Chen, H. M.; Xiao, H.; Li, J.; Huang, Y.; Liu, B. Breaking Long-Range Order in Iridium Oxide by Alkali Ion for Efficient Water Oxidation. *J. Am. Chem. Soc*. **2019**, *141*, 3014−3023.

(29) Zhuang, L.; Ge, L.; Yang, Y.; Li, M.; Jia, Y.; Yao, X.; Zhu, Z. Ultrathin iron-cobalt oxide nanosheets with abundant oxygen vacancies for the oxygen evolution reaction. *Adv. Mater.* **2017**, *29*, 1606793.

(30) Ling, T.; Yan, D.-Y.; Jiao, Y.; Wang, H.; Zheng, Y.; Zheng, X.; Mao, J.; Du, X.-W.; Hu, Z.; Jaroniec, M.; Qiao, S.-Z. Engineering surface atomic structure of single-crystal cobalt (II) oxide nanorods for superior electrocatalysis. *Nat. Commun*. **2016**, 7, 1−8.

(31) Shen, F.-C.;; Wang, Y. Tang, Y.-J.; Li, S.-L.; Wang, Y.-R.; Dong, L. Z.; Li, Y.-F.; Xu, Y.; Lan, Y.-Q. CoV_2O_6–V_2O_5 Coupled with Porous N-Doped Reduced Graphene Oxide Composite as a Highly Efficient Electrocatalyst for Oxygen Evolution. *ACS Energy Lett*. **2017**, *2*, 1327−1333.

(32) Gao, D.; McCrum, T. I.; Deo, S.; Choi, Y.-W.; Scholten, F.; Wan, W.; Chen, G. J.; Janik, J. M.; Cuenya, B. R. A Single-Atom Iridium Heterogeneous Catalyst in Oxygen Reduction Reaction. *Angew. Chem., Int. Ed.* **2019**, *58*, 9640−9645.

(33) Xia, Z.; Zhang, H.; Shen, K.; Qu, Y.; Jiang, Z. Wavelet analysis of extended X-ray absorption fine structure data: Theory, application. *Phys. B* **2018**, *542*, 12−19.

(34) Chen, W.; Pei, J.; He, C.-T.; Wan, J.; Ren, H.; Wang, Y.; Dong, J.; Wu, K.; Cheong, W.-C.; Mao, J.; Zheng, X.; Yan, W.; Zhuang, Z.; Chen, C.; Peng, Q.; Wang, D.; Li, Y. Single Tungsten Atoms Supported on MOF-Derived N-Doped Carbon for Robust Electrochemical Hydrogen Evolution. Adv. Mater. 2018, 30, 1800396.

(35) Huang, Z.-F.; Song, J.; Du, Y.; Xi, S.; Dou, S.; Nsanzimana, J. M. V.; Wang, C.; J. Xu, Z.; Wang, X. Chemical and structural origin of lattice oxygen oxidation in Co–Zn oxyhydroxide oxygen evolution electrocatalysts. *Nat. Energy* **2019**, *4*, 329−338.

(36) Le Goff, A.; Artero, V.; Jousselme, B.; Tran, P. D.; Guillet, N.; Métayé, R.; Fihri, A.; Palacin, S.; Fontecave, M. From hydrogenases to noble metal-free catalytic nanomaterials for H_2 production and uptake. *Science* **2009**, *326*, 1384−1387.

(37) Jaramillo, T. F.; Jørgensen, K. P.; Bonde, J.; Nielsen, J. H.; Horch, S.; Chorkendorff, I. Identification of active edge sites for electrochemical H_2 evolution from MoS_2 nanocatalysts. *Science* **2007**, *317*, 100−102.

(38) Kibsgaard, J.; Chen, Z.; Reinecke, B. N.; Jaramillo, T. F. Engineering the surface structure of MoS_2 to preferentially expose active edge sites for electrocatalysis. *Nat. Chem.* **2012**, *11*, 963−969.

(39) Miao, X.; Zhang, L.; Wu, L.; Hu, Z.; Shi, L.; Zhou, S. Quadruple perovskite ruthenate as a highly efficient catalyst for acidic water oxidation. *Nat. Commun*. **2019**, 10, 1−7.

(40) Laha, S.; Lee, Y.; Podjaski, F.; Weber, D.; Duppel, V.; M. Schoop, L.; Pielnhofer, F.; Scheurer, C.; Müller, K.; Starke, U.; Reuter, K.; V. Lotsch. B. Ruthenium Oxide Nanosheets for Enhanced Oxygen Evolution Catalysis in Acidic Medium. *Adv. Energy Mater.* **2019**, *9*, 1803795.

(41) Kim, J.; Shih, P.-C.; Tsao, K.-C.; Pan, Y.-T.; Yin, X.; Sun, C.-J.; Yang, H. High-Performance Pyrochlore-Type Yttrium Ruthenate Electrocatalyst for Oxygen Evolution Reaction in Acidic Media. *J. Am. Chem. Soc.* **2017**, *139*, 12076−12083.

(42) Yao, Y.; Hu, S.; Chen, W.; Huang, Z.-Q.; Wei, W.; Yao, T.; Liu, R.; Zang, K.; Wang, X.; Wu, G.; Yuan, W.; Yuan, T.; Zhu, B.; Liu, W.; Li, Z.; He, D.; Xue, Z.; Wang, Y.; Zheng, X.; Dong, J.; Chang, C.-R.; Chen, Y.; Hong, X.; Luo, J.; Wei, S.; Li, W.-X.; Strasser, P.; Wu, Y.; Li, Y. Engineering the electronic structure of single atom Ru sites via compressive strain boosts acidic water oxidation electrocatalysis. *Nat. Catal.* **2019**, *2*, 304−313.

(43) Diaz-Morales, O.; Raaijman, S.; Kortlever, R.; J. Kooyman, P.; Wezendonk, T.; Gascon, J.; Fu, W.T.; T.M. Koper, M. Iridium-based double perovskites for efficient water oxidation in acid media. *Nat. Commun*. **2016**, 7, 1−6.

(44) C. Seitz, L.; F. Dickens, C.; Nishio, K.; Hikita, Y.; Montoya, J.; Doyle, A.; Kirk, C.; Vojvodic, A.; Y. Hwang, H.; K. Norskov, J.; F. Jaramillo, T. A highly active and stable IrO_x/$SrIrO_3$ catalyst for the oxygen evolution reaction. *Science* **2016**, *353*, 1011−1014.

(45) Gao, S.; Lin, Y.; Jiao, X.; Sun, Y.; Luo, Q.; Zhang, W.; Li, D.; Yang, J.; Xie, Y. Partially oxidized atomic cobalt layers for carbondioxide electroreduction to liquid fuel. *Nature* **2016**, *529*, 68−71.

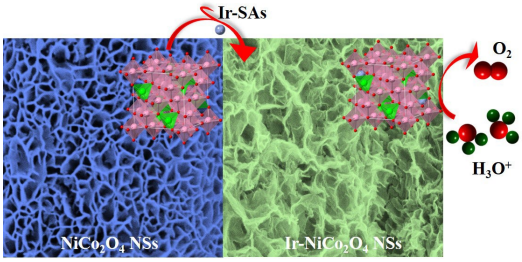
Ir-SAs
O2
H3O+
NiCo2O4 NSs
Ir-NiCo2O4 NSs